Chemical Science

ROYAL SOCIETY OF CHEMISTRY

EDGE ARTICLE

View Article Online
View Journal | View Issue

Cite this: *Chem. Sci.*, 2025, **16**, 7329

All publication charges for this article have been paid for by the Royal Society of Chemistry

Received 23rd December 2024
Accepted 14th March 2025

DOI: 10.1039/d4sc08658a

rsc.li/chemical-science

A Mn–Rh dual single-atom catalyst for inducing C–C cleavage: relay catalysis reversing chemoselectivity in C–H oxidation†

Chang-Jie Yang,[ab] Yu-Da Huang,[b] Yu-Yuan Zhang,[b] Yong-Zhou Pan,[a] Jiarui Yang,[c] Ying-Ming Pan,[b] Tao Gan,[d] Hai-Tao Tang,*[b] Xia Zhang,[a] Wen-Hao Li*[a] and Dingsheng Wang*[c]

The integration of two entirely unrelated organic reactions into a novel reaction poses a formidable challenge. While diatomic catalysts (DACs) have exhibited promise as a framework for realizing this concept, the fusion of disparate organic reactions using DACs remains exceptionally uncommon. The reason for this is that there are often interactions between the two metal sites in DACs, which create new difficulties in catalyst design for already complex reaction systems. Based on this situation, the incorporation of two completely isolated single-atom catalytic systems into the same reaction is a promising solution. Herein, we synthesized a Mn–Rh dual single-atom catalyst (DSAC, Mn_1–Rh_1@O-TiC) and this DSAC demonstrates remarkable selectivity and conversion efficiency in the oxidation reaction of cumene, facilitating the highly efficient production of acetophenone (AP) in an almost quantitative form. The two completely isolated metal catalytic centers, Mn and Rh, each playing a distinct role in the reaction, synergistically propel the directed conversion of cumene to AP in a well-defined manner. This investigation not only illustrates a rare instance of dual single-atom catalyst-mediated relay catalysis in organic synthesis but also imparts valuable insights into the systematic design of catalytic systems for organic tandem reactions, approached from the vantage point in the atomic scale.

Introduction

Single-atom catalysts (SACs) combine the advantages of both homogeneous and heterogeneous catalysts, offering potential catalytic materials with high activity and low cost.[1–5] However, the structure of SACs, being relatively singular, often lacks interatomic synergistic effects.[6,7] Consequently, achieving efficient catalysis in complex reactions solely through modulation of the central metal atom species, atomic coordination structure, and carrier structure remains challenging for SACs.[8–10] To address this limitation and enable synergistic modulation in complex reactions, diatomic catalysts (DACs) with heterogeneous active centers hold significant promise.[11–14] While DACs have found utility in organic synthesis reactions, existing DACs often rely on one atomic site as the primary site, with the other atom providing support through electron perturbation or co-adsorption mechanisms.[15–18] As a result, these catalysts exhibit impressive catalytic efficiency but struggle to influence or control reaction selectivity by altering the reaction pathway.[19–23] In contrast, using two different single-atom catalysts in the same reaction can accommodate two isolated catalytic systems simultaneously, with each single atom performing distinct functions in the catalytic reaction.[24,25] This "division of labor" between the two catalytic sites not only maximizes the utilization of metal atoms but also holds the potential for significant enhancements, or even complete reversals, in product selectivity within complex catalytic systems.[26–29]

The selective activation of inert C(sp^3)–H bonds through oxidative processes presents a significant challenge that researchers worldwide strive to overcome, as it is closely tied to various industrial applications such as the production of phenol and thick-ringed aromatic acids.[30–35] However, the high bond energy and low polarity of C(sp^3)–H bonds make achieving selective oxidative activation under mild conditions thermodynamically and kinetically demanding.[36–39] Among the research areas dedicated to the aerobic oxidation of C(sp^3)–H bonds, the oxidation of cumene holds particular importance in industrial production, as approximately 90% of the world's phenol production relies on this process.[40] In the conventional

[a]*Department of Chemistry, Northeastern University, Shenyang, 110819, P. R. China*
[b]*State Key Laboratory for Chemistry and Molecular Engineering of Medicinal Resources, Key Laboratory for Chemistry and Molecular Engineering of Medicinal Resources (Ministry of Education of China), Collaborative Innovation Center for Guangxi Ethnic Medicine, School of Chemistry and Pharmaceutical Sciences, Guangxi Normal University, Guilin, 541004, P. R. China*
[c]*Department of Chemistry, Tsinghua University, Beijing, 100084, P. R. China*
[d]*Shanghai Synchrotron Radiation Facility, Shanghai Advanced Research Institute, Chinese Academy of Sciences, Shanghai 201204, China*

† Electronic supplementary information (ESI) available. See DOI: https://doi.org/10.1039/d4sc08658a

catalytic cycle, the oxidation of cumene generates a complex mixture of products with various side reactions.[41] The products typically include cumene peroxide (CHP), dimethyl phenyl methanol (BP), and acetophenone (AP) (Fig. 1A).[42] Although the reaction conditions are relatively manageable, the presence of multiple oxidized compounds in the product hampers the desired selectivity.[43,44] As a result, the broader applicability of this process for achieving high selectivity in the production of other value-added products is constrained.[45,46] Addressing these challenges is crucial for advancing the field and enabling the targeted production of desired oxidation products.[47,48] By developing novel catalytic strategies and reaction conditions, it becomes possible to enhance the selectivity and control the reaction pathway, opening doors to the synthesis of high-value products with improved efficiency and purity.[49,50]

In the conventional reaction mechanism, cumene oxidation is typically catalyzed by various non-precious metals, resulting in the formation of a mixture of dimethyl phenyl methanol (BP) and acetophenone (AP), with both compounds present in the product. It has been observed that AP is predominantly generated through two well-known routes: the classical Hayashi route and the cumyl-hydroperoxide route.[51] These routes operate *via* free radical reaction mechanisms, making the production of AP nearly unavoidable in cumene oxidation.[41] In contrast, among classical transition metal-catalyzed C–O bond activation reactions, certain transition metals (such as Fe, Hf, Re, *etc.*) can undergo oxidative addition to the C–O bond of tertiary alcohols, leading to the formation of alkenes through a β-H elimination mechanism (Fig. 1B).[52] Inspired by this observation, we envisioned utilizing the oxidation properties of classical transition metals (M1), known for their strong oxidation-promoting abilities, to facilitate the formation of a mixture of dimethyl phenyl methanol (BP) and acetophenone (AP) from cumene.[53] Subsequently, another metal atom (M2) would employ a β-H elimination mechanism to selectively convert BP into α-substituted styrene (AMS, Fig. 1C).[54] The high olefin oxidation activity of M1

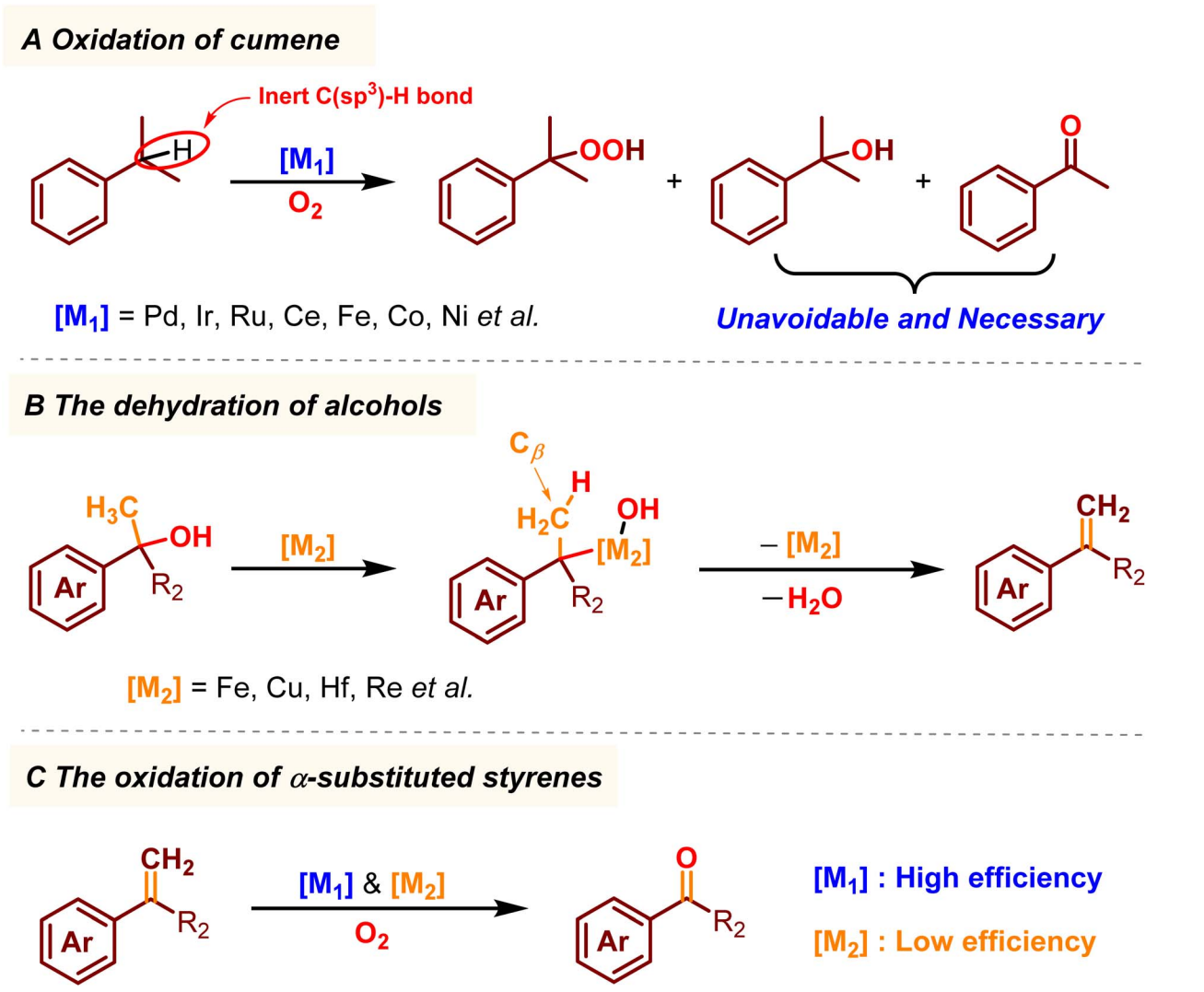

Fig. 1 Research background. (A) Metal meditated oxidation of cumene; (B) the dehydration of alcohols; (C) the oxidation of α-substituted styrenes.

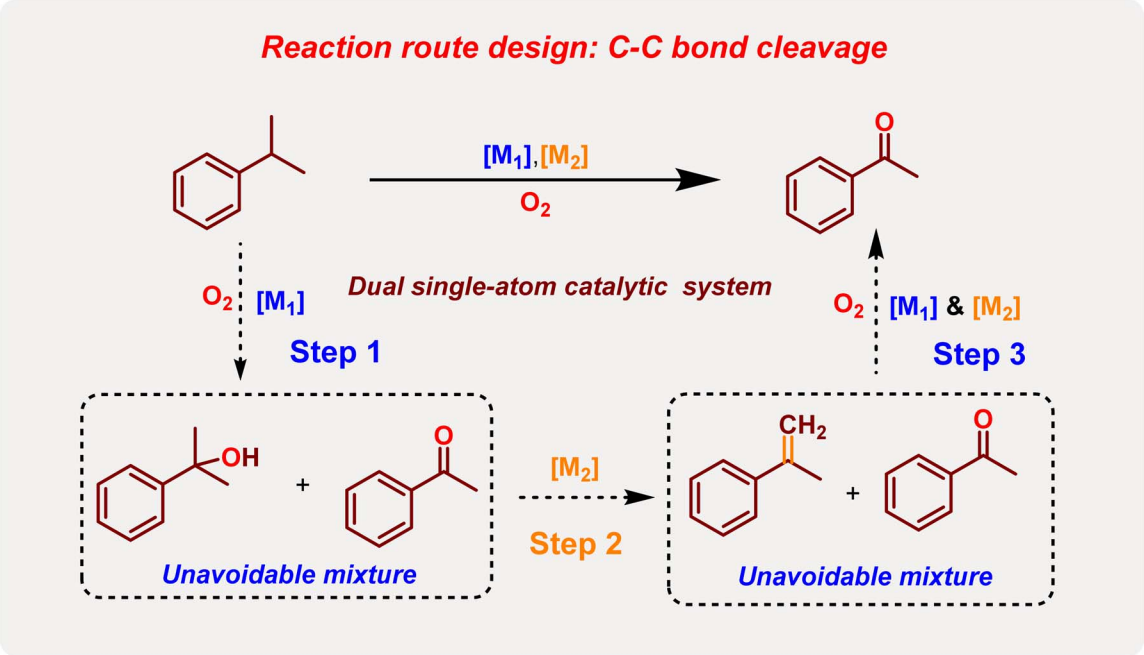

Fig. 2 The design of the cumene oxidation reaction route.

would accelerate the cleavage of olefin functional groups, ultimately enabling the production of AP with exceptionally high selectivity (Fig. 2).[55] By implementing this innovative dual single-atom catalytic approach, we aim to reverse the typical chemoselectivity observed in inert C–H bond oxidation, instead favoring the pathway of C–C bond cleavage.[56]

Results and discussion

To achieve highly selective conversion of cumene to acetophenone (AP), it is essential to construct a single-atom catalyst (SAC) with high reactivity towards cumene oxidation. In our study, we conducted a high-throughput screening of SACs supported by oxides, carbides and nitrides (Fig. 3B and ESI Tables S1–S10†). The screening results revealed that transition metal manganese (Mn) catalysts exhibited superior efficiency, enabling smooth catalysis of the cumene oxidation reaction with various Mn-based SACs. Classical Mn SACs supported by oxides typically exhibit a localized reactivity center with a Mn-Ox-M basic coordination structure. However, we observed that Mn_1@TiN, with a Mn–Nx coordination structure, displayed lower reactivity in the reaction. This highlights the necessity of the Mn-Ox-M basic coordination structure for optimal catalytic performance. Considering that the oxygen-treated TiC surface could potentially exhibit a similar coordination structure to metal oxides, we speculated that oxygen-treated titanium carbide might facilitate efficient conversion in the reaction. We subjected the TiC support to a simple treatment involving concentrated alkali, resulting in the formation of a uniform layer of reactive oxygen atoms/hydroxyl groups on its surface. The Mn atoms were trapped by the hydroxyl groups on the surface of the alkali-treated TiC, forming stable Mn-Ox-Ti active sites after the release of a molecule of HCl. After impregnation and heating, Mn atoms were uniformly anchored onto the support surface. Among the various catalyst formulations tested, we found that the best catalytic performance was achieved when Mn was loaded onto the surface of the oxygen-modified TiC support (Mn_1@O-TiC). This catalyst formulation enabled the conversion of all feed-stocks into a mixture of dimethyl phenyl methanol (BP) and acetophenone (AP) with nearly quantitative yields within a 12-hour reaction period (up to 98% conversion with a selectivity of 52% for AP). The successful development of the Mn_1@O-TiC catalyst demonstrates the significance of tailored SAC design and the importance of the Mn-Ox-Ti coordination structure in achieving highly efficient and selective cumene oxidation. This catalytic system holds great promise for the synthesis of AP with exceptional yields and selectivity.

Based on these results, we then directed our research towards the design and construction of DSACs (Fig. 3C, ESI Tables S11 and S12†). Initially, considering the cost of the catalyst, we synthesized a dual single-atom catalyst (Mn–Fe DSAC). While the reaction maintained a good overall yield, the catalyst selectivity not only failed to improve but also decreased to 38%. In contrast, Hf, which had shown promise in previous studies, emerged as the most favorable and operationally feasible metal precursor for promoting the successful dehydration of dimethyl phenyl methanol (BP) into acetophenone (AP). Introducing Hf into the single-atom catalytic system led to a remarkable improvement in the reaction selectivity, reaching 95%. However, regrettably, this modification also caused a decrease in the overall yield to 70%. Motivated by these findings, we shifted our focus to precious metals such as Pd, Ir, and Rh. To our excitement, the Mn_1–Rh_1@O-TiC catalyst

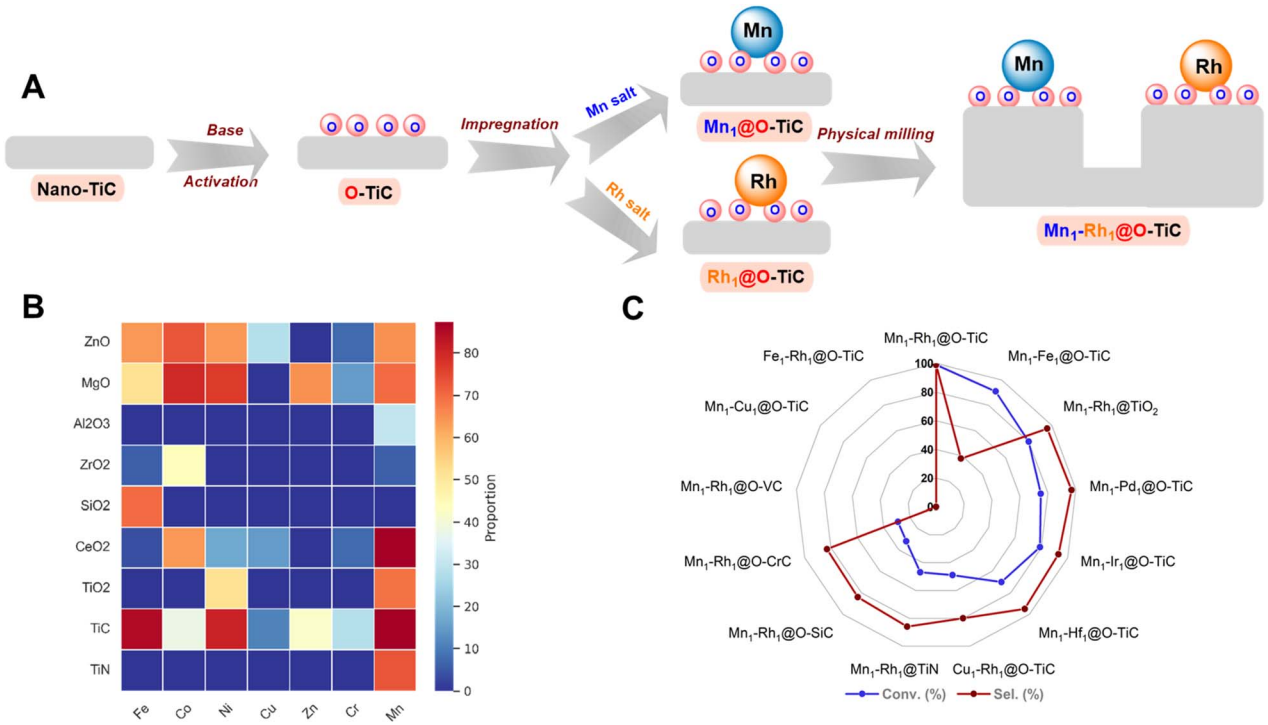

Fig. 3 Synthesis and optimization of catalysts. (A) Schematic synthetic procedure of the dual single-atom catalyst. (B) Heat map for high-throughput screening of SACs. (C) Radar chart for dual single-atom catalyst screening.

(Fig. 3A) demonstrated exceptional performance. Incorporating Rh as the second metal species in the catalyst allowed us to maintain high conversion in the reaction while achieving an outstanding selectivity of 99% for AP. Ultimately, we explored the grinding ratio of the two metals, which was suggested to strongly influence the catalytic performance, and found that the optimal catalytic activity and selectivity were achieved when the mass ratio of Mn to Rh was 10 : 1 (ESI Table S17†).

After achieving the desired catalytic outcomes, it became crucial to verify whether the catalyst structure aligned with our initial vision for a dual single-atom catalyst. To address this, we conducted meticulous characterization of the catalyst. In the classical impregnation method for synthesizing SACs with oxide supports, the metal-loading of SACs is often very low due to the lack of strong metal–support interactions. Inductively coupled plasma atomic emission spectrometry (ICP-AES) analysis revealed that the Mn loading in the Mn_1–Rh_1@O-TiC catalyst was 0.93 wt%, while the Rh loading was 0.61 wt% (ESI Table S19†). This indicates that a stable M–O interaction has indeed formed between the metal atoms and the support in the Mn_1–Rh_1@O-TiC catalyst, rather than simple physical mixing/adsorption. Transmission electron microscopy (TEM) and high-resolution transmission electron microscopy (HR-TEM) images of Mn_1–Rh_1@O-TiC confirmed the absence of cluster or nanoparticle formation during the catalyst's preparation and synthesis (ESI Fig. S2 and S3†). Elemental energy dispersive spectroscopy (EDS) mapping of the oxygen-treated TiC (O-TiC) supports indicated that the surface of the support had undergone oxidative modification by alkali treatment. Furthermore, EDS mapping of the catalysts demonstrated the uniform distribution of Rh and Mn elements on the O-TiC support surface (ESI Fig. S4†). Additionally, spherical aberration-corrected high-angle annular dark-field scanning transmission electron microscopy (AC-HAADF-STEM) images revealed only a small number of isolated bright spots diffused within the material, with no aggregation of bright spots, indicating the absence of Mn or Rh clusters or nanoparticles (Fig. 4G). X-ray diffraction (XRD) analysis of the catalyst showed no peaks corresponding to manganese or rhodium nanoparticles (ESI Fig. S11 and S12†), consistent with the results obtained from various electron microscopy characterization studies.

In accordance with the K-edge X-ray absorption near-edge structure (XANES, Fig. 4A) spectra of Rh for Mn_1–Rh_1@O-TiC, the valence state of Rh in the catalyst differs significantly from that in Rh foil and Rh_2O_3, suggesting a unique structure distinct from both samples. The intensity of the absorption edge and the white line peak of Rh in the catalyst is more similar to that of the Rh_2O_3 sample, indicating that its oxidation state is closer to +3, which agrees with the results from XPS (ESI Fig. S13 and S14†).

The X-ray photoelectron spectroscopy (XPS) analysis of the Ti 2p peak at ~458.4 eV provides clear evidence of prominent Ti–O bonds in the catalyst. This observation implies effective oxidation of the titanium carbide surface, as corroborated by the ESI (Fig. S13).† A similar pattern is discernible in the XPS analysis of O 1s. To delve into the microscopic coordination environments of Rh within the catalyst, extended X-ray absorption fine structure (FT-EXAFS) fitting analysis was employed, revealing a major peak at 1.5 Å corresponding to Rh–O scattering (Fig. 4B).

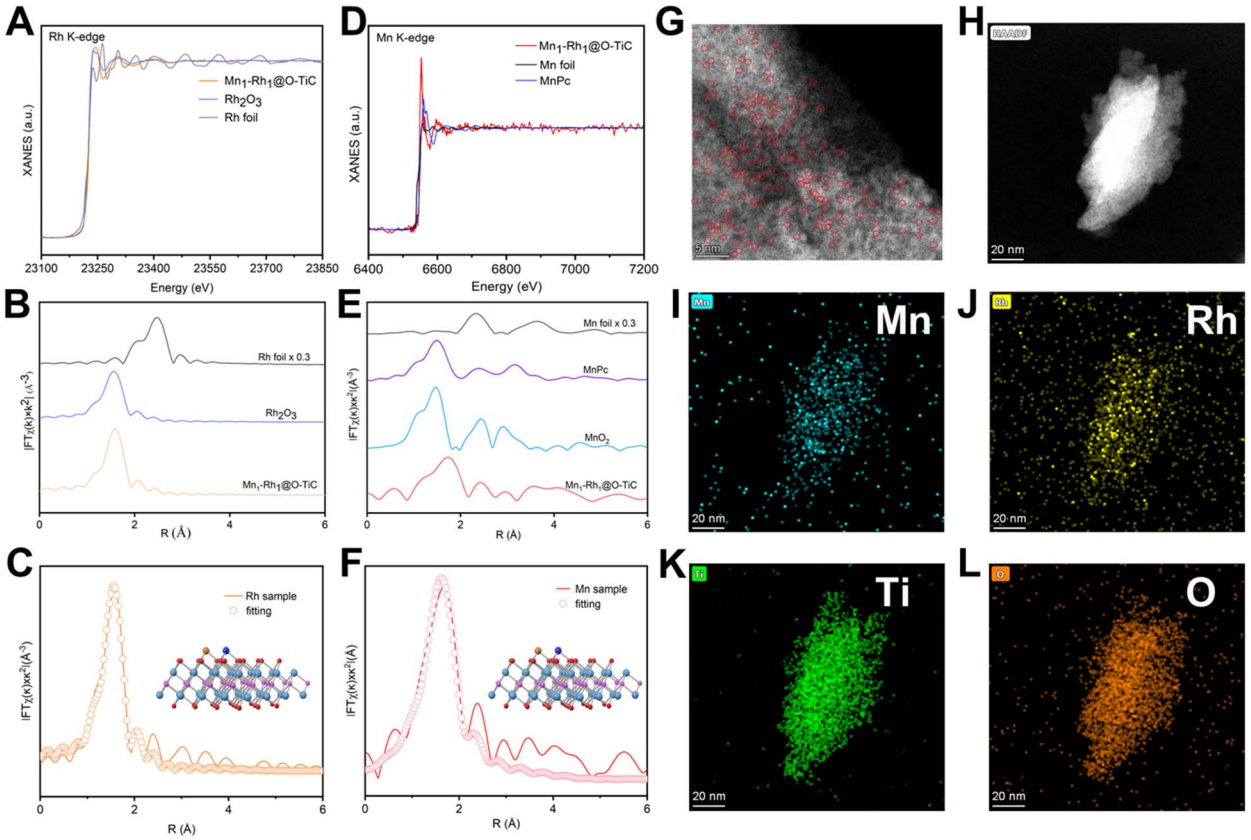

Fig. 4 Structural characterization studies. (A) XANES of Rh foil, Rh_2O_3, and Mn_1–Rh_1@O-TiC. (B) FT-EXAFS of Rh foil, Rh_2O_3, and Mn_1–Rh_1@O-TiC. (C) Rh K-edge EXAFS fitting analysis of the Rh-sample in *R* space. (D) XANES of Mn foil, MnPc, and Mn_1–Rh_1@O-TiC. (E) FT-EXAFS of Mn foil, MnO_2, MnPc, and Mn_1–Rh_1@O-TiC. (F) Mn K-edge EXAFS fitting analysis of the Mn-sample in *R* space. (G) AC-HAADF-STEM of Mn_1–Rh_1@O-TiC. (H–L) EDX spectroscopy mapping of Mn_1–Rh_1@O-TiC.

Further scrutiny, detailed in Fig. 4C and ESI Table S20,† indicates that the Rh atom is coordinated with four O atoms. Wavelet transforms (WTs) of the X-ray absorption spectroscopy (XAS) results (ESI Fig. S18†) also exhibit distinctive Rh–O scattering. We investigated the microscopic coordination environment of the Mn atom in the Mn–Rh catalytic system using X-ray absorption fine structure (XAFS) spectroscopy. The K-edge X-ray absorption near-edge structure (XANES) spectra (Fig. 4D) reveal that the oxidation state of Mn in the catalytic system differs significantly from that of Mn in foil and MnPc, falling within the range of 0 to +2, with a closer alignment to +2. FT-EXAFS shows two distinct signal peaks at 1.75 Å and 2.42 Å, attributed to Mn–O and Mn–O–Ti scattering, respectively (Fig. 4E). The XAS results of the WTs revealed distinct Mn–O scattering features, whereas no Mn–Mn scattering signal was detected (ESI Fig. S19†). Furthermore, FT-EXAFS fitting indicates that the average coordination number (CN) of Mn–O in the Mn–Rh catalytic system is four (Fig. 4F and ESI Table S21†). Nevertheless, the closely aligned atomic numbers of Mn and Ti, coupled with Mn's marginally higher K-edge energy compared to Ti, give rise to significant interference of Mn atoms by Ti during synchrotron radiation and spherical aberration electron microscopy characterization.

In response to this challenge, we employed X-ray diffraction (XRD) (ESI Fig. S10 and S11†) and conducted energy-dispersive X-ray spectroscopy mapping in AC HAADF-STEM (Fig. 4H–L) to concisely demonstrate their atomic dispersion states. To gain insights into the microscopic coordination environment of Mn atoms, we optimized the structure of the Mn SAC by mimicking the coordination structure of the Rh SAC through the first-principles calculations. We simulated the microscopic coordination state of Mn single atoms on O-TiC. Computational optimization results reveal that, in the initial state, Mn atoms coordinate with three oxygen atoms and undergo self-oxidation under oxygen conditions. This process leads to the formation of Mn═O bonds, ultimately resulting in the establishment of a stable Mn–O4 coordination structure.

To discern the specific contributions of Mn and Rh atoms in the catalyst to the reaction, a series of validation experiments were conducted (ESI Tables S15, S16 and S23†). Rh atoms loaded on O-TiC were prepared to elucidate their roles in various reaction steps. Application of these catalysts to the cumene oxidation reaction, with a reduced reaction time of 2 hours, revealed the presence of both BP and AMS intermediates through liquid phase-high resolution mass spectrometry. This suggests that the Rh catalyst may play a pivotal role in the BP dehydration step. Substantiating this hypothesis, using BP as

the reactant under standard conditions yielded both AMS and AP at the end of the reaction, emphasizing the criticality of the AP dehydration step in the catalytic cycle. With the elevated catalytic efficiency of the Mn SAC, it can rapidly and non-selectively promote the generation of mixed products. In contrast, controlled experiments reveal a sluggish catalytic efficiency for Rh catalysts in catalyzing the direct oxidation of cumene. This observation suggests that the key to promoting the reaction to produce BP with high selectivity lies in the continuous and highly selective dehydration and oxidation of AP, which is rapidly accumulated in the reaction by the Mn catalyst. Additionally, to verify the distinct reaction pathways of our catalyst, we conducted electron paramagnetic resonance (EPR) experiments on the cumene oxidation reaction (Fig. 5D). The experimental results revealed that the presence of single linear oxygen ($^1O_2$) was detected, but not ·OOH radical species. This result is obviously different from the classical ·OOH-induced radical deprotonation process,[57] which is one of the keys to achieve a significant improvement in the catalytic performance.

Based on the above control experimental results and the classical reaction mechanism,[58] we propose the following mechanism for the oxidation of cumene (CM) to acetophenone (AP): first, the catalyst facilitates the activation of oxygen to generate singlet oxygen ($^1O_2$), which abstracts hydrogen atoms from CM to form tertiary carbon radical species (confirmed by HPLC-MS detection). These radicals are then converted into BP under the influence of the catalyst. Subsequently, BP undergoes

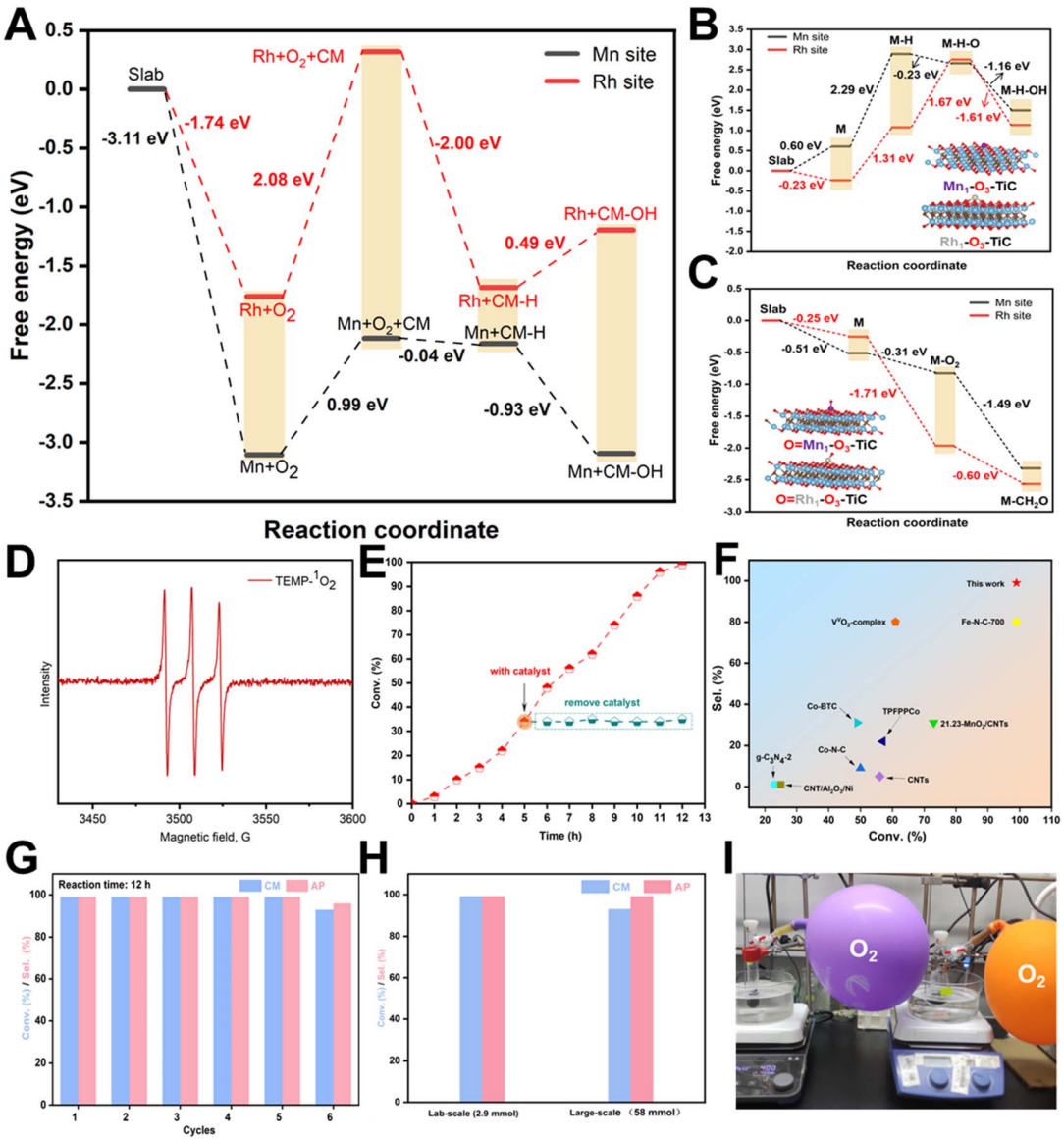

Fig. 5 First-principles calculation diagrams and catalytic performance. (A) The conversion of CM to BP. (B) Dimethyl phenyl methanol dehydration. (C) α-Methyl styrene oxidation cleavage (purple: Mn, gray: Rh, blue: Ti, brown: C, and red: O). (D) EPR experiment. (E) Hot filtration test. (F) Comparison of activity for the Mn–Rh DSAC with other reported catalytic systems.[35,39,41,53,59–62] (G) Cycle experiment. (H) The corresponding catalytic results (lab-scale, left and large-scale, right). (I) Photograph showing lab-scale (2.9 mmol, left) and scale-up (58 mmol, right) reactions.

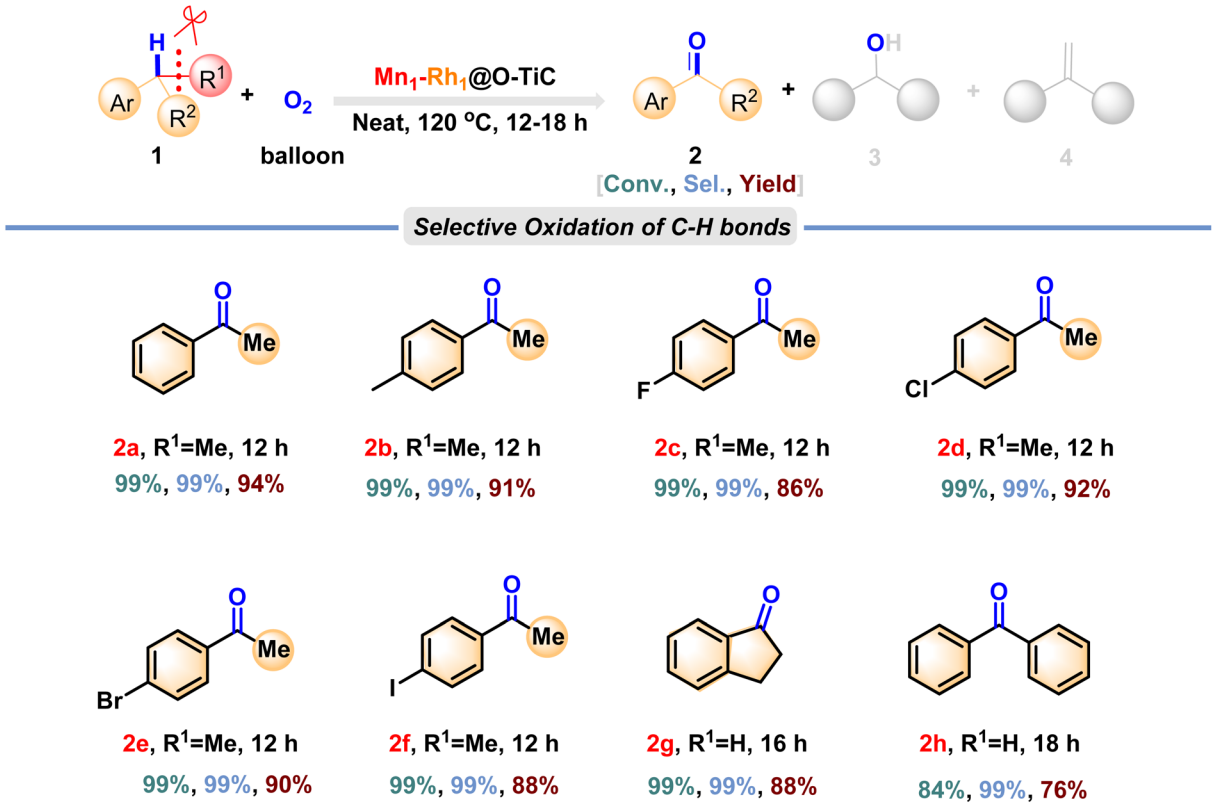

Fig. 6 Selective oxidation of C(sp^3)–H bonds with Mn_1–Rh_1@O-TiC as a catalyst. Reaction conditions: 40 mg of catalyst (0.08 mol%), 2.9 mmol of substrates, 120 °C for 12–18 h, isolated yield.

a dehydration reaction to form AMS (confirmed by HPLC-MS detection), which ultimately undergoes oxidative cleavage to generate AP (confirmed by HPLC-MS detection). To further validate this reaction mechanism and elucidate the specific role of the catalyst in the catalytic cycle, we conducted first-principles calculations on the reaction network. As shown in the free energy diagram, the oxidation of CM to BP proceeds through four steps: oxygen adsorption, CM adsorption, hydrogen atom transfer from CM, and hydroxyl group transfer (Fig. 5A). Among these, the rate-determining step is the adsorption of cumene (for the structures of the reaction intermediates, refer to Fig. S15†). For Mn atoms, the energy barrier for cumene adsorption is relatively low (0.99 eV), whereas for Rh atoms, it is significantly higher (2.08 eV). This indicates that Mn atoms facilitate the conversion of CM to BP more effectively than Rh atoms. The dehydration process of BP consists of four main steps: adsorption of BP (**M**), dissociation of the hydroxyl group in the substrate at the metal catalytic center (**M–H**), dissociation of oxygen from the substrate hydroxyl group (**M–H–O**), and dissociation of the β-position C–H bond after the dissociation of the hydroxyl group on the substrate (**M–H–OH**) (Fig. 5B). For Mn atoms, the rate-determining step is **M–H**, with an energy barrier of 2.29 eV. In contrast, for Rh atoms, hydroxyl hydrogen dissociation occurs more easily, making **M–H–O** the rate-determining step, with a significantly lower energy barrier of 1.67 eV (for the structures of the reaction intermediates, refer to Fig. S16†). AMS oxidative cleavage is a highly exothermic reaction that involves three main steps: AMS adsorption (**M**), O_2 activation (**M–O_2**), and AP formation (**M–CH_2O**) following molecular adsorption (Fig. 5C). For Rh atoms, the rate-determining step is AP formation, with an energy barrier of −1.49 eV, whereas for Mn atoms, the rate-determining step is O_2 activation (**M–O_2**), which has a relatively higher energy barrier of −1.71 eV (for the structures of the reaction intermediates, refer to Fig. S17†). Therefore, compared to Mn atoms, Rh atoms are more favorable for facilitating both BP dehydration and AMS oxidative cleavage.

To fully comprehend the intrinsic relationship between catalysts and reactions, we embarked on exploring the practical applications of this dual single-atom catalyst. An essential characteristic of heterogeneous catalytic systems is their reusability. To assess this, we conducted multiple cycles of cumene oxidation using the Mn_1–Rh_1@O-TiC catalyst under an O_2 atmosphere (1 atm). After each run, the Mn–Rh DSAC was recovered through vacuum evaporation and underwent sequential washing with methanol, ethyl acetate, and deionized water. Remarkably, the conversion and selectivity (AP) of the reaction remained consistently high for up to 6 cycles (Fig. 5G). These findings demonstrate that the catalyst not only possesses the fundamental attributes of a heterogeneous catalytic system but also retains excellent stability across multiple reaction cycles. Building upon these promising results, we sought to

assess the viability of this catalytic system in large-scale applications, with a focus on exploring its potential for industrial production. We scaled up the cumene oxidation reaction to a volume of 58 mmol (expanded by a factor of 20 compared to the amount of substrate used in the laboratory test), and the experimental outcomes were highly encouraging. The catalytic system successfully produced acetophenone (AP) with a conversion rate of 90% and a selectivity of 99% (Fig. 5H and I), underscoring its potential for industrial implementation. These results underscore the practicality and scalability of the Mn–Rh catalyst, further highlighting its potential for diverse industrial applications. It's worth mentioning that the hot filtration test and ICP-AES measurements demonstrate that there were no manganese and rhodium leaching during the reaction (Fig. 5E and ESI Table S19†). Meanwhile, we found that the catalytic efficiency of Mn–Rh catalytic system-mediated tandem catalysis in the oxidation process of cumene was significantly higher than that of other similar catalysts that have been reported (including metal complexes, transition-metal catalysts, and inorganic non-metallic materials, Fig. 5F and ESI Table S18†).

The remarkable performance of the Mn_1–Rh_1@O-TiC catalyst has also been extended to probe the selective oxidation of a wide range of inert C–H bonds under cumene oxidation conditions (Fig. 6). Isopropyl benzene containing a variety of substituents (*e.g.*, methyl and halogen) was successfully converted to the corresponding ketones (**2b–2f**, respectively) with high conversion (>85%) and high selectivity (up to 99%), and good to excellent yields (86–94%) could be obtained. In addition, the benzene heterocyclic molecule indan was also tolerated and 2,3-dihydro-1*H*-inden-1-one (**2g**) was obtained with excellent conversion (99%), selectivity (99%), and yield (92%). It is noteworthy that this dual single-atom catalyst was also able to activate the sterically hindered substrate diphenylmethane smoothly and with high conversion (84%) and selectivity (99%) to obtain benzophenone (**2h**) in 76% yield.

Conclusions

In summary, we have successfully engineered a multifunctional dual single-atom catalyst (Mn_1–Rh_1@O-TiC), and Mn_1–Rh_1@O-TiC exhibits precise promotion of each oxidation step in the cumene oxidation process through distinct metal active centers. This enables the establishment of a novel chemical oxidation pathway for cumene, resulting in the efficient and highly selective production of oxidized acetophenone (AP) products. Through a comprehensive series of mechanism validation experiments and theoretical calculations, we have elucidated the individual roles of the Mn SAC and Rh SAC components within the catalytic system. Specifically, the Mn SAC component facilitates the rapid and effective oxidation of cumene, yielding dimethyl phenyl methanol (BP) and AP. Concurrently, the Rh SAC component catalyzes the dehydration of BP, generated in the Mn SAC-mediated process, to produce α-methyl styrene (AMS). Notably, the synergistic catalysis of the Mn SAC and Rh SAC leads to the swift oxidation and cracking of AMS, ultimately converting it into AP. Throughout the entire reaction sequence, the two metal catalytic centers within the catalyst perform distinct yet complementary roles, working in relay to catalyze the overall reaction with a high degree of selectivity. The dual single-atom catalyst not only exhibits excellent selectivity (>99%) but also achieves considerable catalytic activity in the oxidation of cumene. The reaction achieves 99% conversion and 94% separation yield, with the turnover number (TON) calculated to be 1152. Moreover, it demonstrates comparable efficacy in other highly selective oxidation reactions involving inert C(sp^3)–H bonds. This work not only marks a significant achievement in realizing rare DSAC-mediated relay catalysis in organic synthesis but also contributes valuable insights into the rational design of catalytic systems for organic relay catalysis reactions, offering a fresh perspective from the realm of inorganic chemistry.

Data availability

The data supporting this article have been included as part of the ESI.†

Author contributions

Li, W. H.; Tang, H. T.; and Wang, D. conceived the idea, designed the study, planned the synthesis, and acquired funding. Li, W. H. and Yang, C. J. analyzed the data and wrote the paper. Yang, C. J., Huang, Y. D., Zhang, X., Yang, J. and Pan, Y. Z. synthesized and characterized the catalysts. Pan, Y. M. carried out the theoretical calculation.

Conflicts of interest

The authors declare no competing financial interest.

Acknowledgements

This work was supported by the NSFC (22401038, 22325101, 22388102, 223B2902, and 22201049), the National Key R&D Program of China (2023YFA1506801), Beijing Natural Science Foundation (Z240027), Guangxi Natural Science Foundation of China (2021GXNSFFA220005), the Ba-Gui Youth Top-notch Talents Project of Guangxi, and the National High-Level Personnel of Special Support Program for Young Top-notch Talents (9th batch). W.-H. L. was supported by the Liaoning Revitalization Talents Program (China, XLYC2403076) and the Young Elite Scientists Sponsorship Program by the Chinese Chemical Society. We acknowledge technical support at the 1W1B beamline of the Advanced Photon Source in BL11B station at the Shanghai Synchrotron Radiation Facility. Besides, special thanks to the Analytical and Testing Center, Northeastern University, for providing instruments.

References

1 B. Qiao, A. Wang, X. Yang, L. F. Allard, Z. Jiang, Y. Cui, J. Liu and T. Zhang, *Nat. Chem.*, 2011, **3**, 634–641.
2 Z. Chen, J. Liu, M. J. Koh and K. P. Loh, *Adv. Mater.*, 2022, **34**, 2103882.

3 S. K. Kaiser, Z. Chen, D. F. Akl, S. Mitchell and J. Pérez-Ramírez, *Chem. Rev.*, 2020, **120**, 11703–11809.
4 B. S. Manoj, B. Gawande, A. D. Kute, R. S. Varma, P. Fornasiero, P. McNeice, R. V. Jagadeesh, M. Beller and R. Zbořil, *Chem. Rev.*, 2021, **121**, 13620–13697.
5 F. Xie, X. Cui, X. Zhi, D. Yao, B. Johannessen, T. Liu, J. Tang, T. B. F. Woodfield, L. Gu and S. Qiao, *Nat. Synth.*, 2023, **2**, 129–139.
6 T. Gan and D. Wang, *Nano Res.*, 2024, **17**, 18–38.
7 W. H. Li, J. Yang, H. Jing, J. Zhang, Y. Wang, J. Li, J. Zhao, D. Wang and Y. Li, *J. Am. Chem. Soc.*, 2021, **143**, 15453–15461.
8 B. C. Ye, W. H. Li, X. Zhang, J. Chen, Y. Gao, D. Wang and G. H. Pan, *Adv. Mater.*, 2024, 2402747.
9 V. B. Saptal, V. Ruta, M. A. Bajada and G. Vilé, *Angew. Chem., Int. Ed.*, 2023, **62**, e202219306.
10 Y. Gao and D. Wang, *CCS Chem.*, 2024, **6**, 833–855.
11 W. Zhang, Y. Chao, W. Zhang, J. Zhou, F. Lv, K. Wang, F. Lin, H. Luo, J. Li, M. Tong, E. Wang and S. Guo, *Adv. Mater.*, 2021, **33**, 2102576.
12 W. H. Li, J. Yang and D. Wang, *Angew. Chem., Int. Ed.*, 2022, **61**, e202213318.
13 S. Ning, H. Ou, Y. Li, C. Lv, S. Wang, D. Wang and J. Ye, *Angew. Chem., Int. Ed.*, 2023, **62**, e202302253.
14 X. Zheng, J. Yang, P. Li, Z. Jiang, P. Zhu, Q. Wang, J. Wu, E. Zhang, W. Sun, S. Dou, D. Wang and Y. Li, *Angew. Chem., Int. Ed.*, 2023, **62**, e202217449.
15 R. Li, Z. Zhang, X. Liang, J. Shen, J. Wang, W. Sun, D. Wang, J. Jiang and Y. Li, *J. Am. Chem. Soc.*, 2023, **145**, 16218–16227.
16 J. Fu, J. Dong, R. Si, K. Sun, J. Zhang, M. Li, N. Yu, B. Zhang, M. G. Humphrey, Q. Fu and J. Huang, *ACS Catal.*, 2021, **11**, 1952–1961.
17 X. Hai, Y. Zheng, Q. Yu, N. Guo, S. Xi, X. Zhao, S. Mitchell, X. Luo, V. Tulus, M. Wang, X. Sheng, L. Ren, X. Long, J. Li, P. He, H. Lin, Y. Cui, X. Peng, J. Shi, J. Wu, C. Zhang, R. Zou, G. Guillén-Gosálbez, J. Pérez-Ramírez, M. J. Koh, Y. Zhu, J. Li and J. Lu, *Nature*, 2023, **622**, 754–760.
18 L. Zhang, T. Li, X. Dai, J. Zhao, C. Liu, D. He, K. Zhao, P. Zhao and X. Cui, *Angew. Chem., Int. Ed.*, 2023, **62**, e2023133.
19 P. Deng, J. Duan, F. Liu, N. Yang, H. Ge, J. Gao, H. Qi, D. Feng, M. Yang, Y. Qin and Y. Ren, *Angew. Chem., Int. Ed.*, 2023, **62**, e202307853.
20 L. Liu and A. Corma, *Chem. Rev.*, 2023, **123**, 4855–4933.
21 W.-H. Li, J. Yang, D. Wang and Y. Li, *Chem*, 2022, **8**, 119–140.
22 Y. Chai, S. Chen, Y. Chen, F. Wei, L. Cao, J. Lin, L. Li, X. Liu, S. Lin, X. Wang and T. Zhang, *J. Am. Chem. Soc.*, 2023, **146**, 263–273.
23 H. Liu, P. Zhu, D. Yang, C. K. Zhong, J. l. Li, X. Liang, L. Wang, H. Yin, D. Wang and Y. Li, *J. Am. Chem. Soc.*, 2024, **146**(3), 2132–2214.
24 C. Liu, T. Li, X. Dai, J. Zhao, D. He, G. Li, B. Wang and X. Cui, *J. Am. Chem. Soc.*, 2022, **144**, 4913–4924.
25 Y. P. Yun, P. Rao, H. L. Sheng, Y. N. Shi, Y. A. Zhu, S. C. Wang, K. K. Li, B. Zhang, T. Yao, H. T. Sheng, H. Z. Yu and M. Z. Zhu, *Adv. Mater.*, 2024, **36**, 2409436.
26 M. H. Tang, J. Shen, Y. D. Wang, Y. F. Zhao, T. Gan, X. S. Zheng, D. Wang, B. X. Han and Z. M. Liu, *Nat. Commun.*, 2024, **15**, 5630.
27 J. Sun, L. Tao, C. Ye, Y. Wang, G. Meng, H. Lei, S. Zheng, C. Xing, X. Tao, P. Wu, J. Chen, S. Du, D. Wang and Y. Li, *J. Am. Chem. Soc.*, 2023, **145**, 7113–7122.
28 B. Jaleh, A. Nasri, M. Eslamipanah, M. Nasrollahzadeh, M. Daneshnazar, J. H. Advani, P. Fornasiero, R. Zbořil, M. Antonietti and M. B. Gawande, *Appl. Catal., B*, 2011, **33**, 2106371.
29 Y. Wang, F. Ma, G. Zhang, J. Zhang, H. Zhao, Y. Dong and D. Wang, *Nano Res.*, 2024, **17**, 9397–9427.
30 M. Wang, J. Wen, Y. Huang and P. Hu, *ChemSusChem*, 2021, **14**, 5049–5056.
31 X. Cao, Z. Chen, R. Lin, W.-C. Cheong, S. Liu, J. Zhang, Q. Peng, C. Chen, T. Han, X. Tong, Y. Wang, R. Shen, W. Zhu, D. Wang and Y. Li, *Nat. Catal.*, 2018, **1**, 704–710.
32 G. Zhang, Z. Zhang and R. Zeng, *Chin. J. Chem.*, 2021, **39**, 3225–3230.
33 J. Wu, J. Chen, Y. Lei, L. Wang, H. Zhu, R. Liu, G. Song, C. Feng and Y. Li, *Green Chem.*, 2023, **25**, 940–945.
34 J. Liu, W. Zhao, L. Lu, Y. Liu, Y. Chen and W. Xiao, *Green Synth. Catal.*, 2021, **2**, 389–392.
35 W. Liu, L. Zhang, X. Liu, X. Liu, X. Yang, S. Miao, W. Wang, A. Wang and T. Zhang, *J. Am. Chem. Soc.*, 2017, **139**, 10790–10798.
36 Y. Liu, Y. Zheng, D. Feng, L. Zhang, L. Zhang, X. Song and Z. A. Qiao, *Angew. Chem., Int. Ed.*, 2023, **62**, e20230626.
37 C. Mu, Y. Cao, H. Wang, H. Yu and F. Peng, *Chem. Eng. Sci.*, 2018, **177**, 391–398.
38 C. Mu, K. Huang, T. Cheng, H. Wang, H. Yu and F. Peng, *Chem. Eng. J.*, 2016, **306**, 806–815.
39 Z. Chen, Y. Deng, G. Yang, Y. N. Zhu, Q. Zhang, Z. Liu, Y. Cao and F. Peng, *ACS Sustainable Chem. Eng.*, 2023, **11**, 5773–5781.
40 S. Liao, Y. Chi, H. Yu, H. Wang and F. Peng, *ChemCatChem*, 2014, **6**, 555–560.
41 H. M. Shen, M. Y. Hu, L. Liu, B. Qi, H. L. Ye and Y. B. She, *Appl. Catal., A*, 2020, **599**, 117599.
42 C.-O. L. Crites, G. L. Hallett-Tapley, M. Frenette, M. González-Béjar, J. C. Netto-Ferreira and J. C. Scaiano, *ACS Catal.*, 2013, **3**, 2062–2071.
43 Z. Xue, J. Yang, L. Ma, H. Li, L. Luo, K. Ji, Z. Li, X. Kong, M. Shao, L. Zheng, M. Xu and H. Duan, *ACS Catal.*, 2023, **14**, 249–261.
44 H. Wang, C. Cao, D. Li, Y. Ge, R. Chen, R. Song, W. Gao, X. Wang, X. Deng, H. Zhang, B. Ye, Z. Li and C. Li, *J. Am. Chem. Soc.*, 2023, **145**, 16852–16861.
45 P. Majumder, A. Basak, H. Kuiry, H. S. Sasmal, S. Karak, P. Saha, B. Chandra, S. Sen Gupta and R. Banerjee, *J. Am. Chem. Soc.*, 2023, **145**, 18855–18864.
46 D. P. Hruszkewycz, K. C. Miles, O. R. Thiel and S. S. Stahl, *Chem. Sci.*, 2017, **8**, 1282–1287.
47 H. Zhu, J. Zhao, Z. Yu, J. Li, C. Ma, H. Sun, Y. Wu and Q. Meng, *Ind. Eng. Chem. Res.*, 2023, **62**, 8253–8268.
48 Z. Yin, Z. Gao, L. Luo, X. Zhang, W. Hou, W. Dai, S. Tian, X. Qin, M. Wang, M. Peng, K. Li, S. Wang, L. Zhang, H. Wang, J. Li, Q. Zhu, B. Cheng, Z. Yin and D. Ma, *Angew. Chem., Int. Ed.*, 2024, e202415044.

49 J. Yang, W. H. Li, H. T. Tang, Y. M. Pan, D. Wang and Y. Li, *Nature*, 2023, **617**, 519–523.
50 S. Tian, B. Wang, W. Gong, Z. He, Q. Xu, W. Chen, Q. Zhang, Y. Zhu, J. Yang, Q. Fu, C. Chen, Y. Bu, L. Gu, X. Sun, H. Zhao, D. Wang and Y. Li, *Nat. Commun.*, 2021, **12**, 3181.
51 K. E. Kharlampidi, T. S. Nurmurodov, N. V. Ulitin, K. A. Teresh-chenko, N. P. Miroshkin, D. A. Shiyan, N. A. Novikov, O. V. Stoyanov, N. N. Ziyatdinov, T. V. Lapteva and S. L. Khursan, *Chem. Eng. Process.*, 2021, **161**, 108314.
52 D. J. Ward, D. J. Saccomando, G. Walker and S. M. Mansell, *Catal. Sci. Technol.*, 2023, **13**, 2638–2647.
53 J. Jiang, R. Luo, X. Zhou, F. Wang and H. Ji, *Mol. Catal.*, 2017, **440**, 36–42.
54 J. Li, A. Das, Q. Ma, M. J. Bedzyk, Y. Kratish and T. J. Marks, *ACS Catal.*, 2022, **12**, 1247–1257.
55 A. Gonzalez-de-Castro and J. Xiao, *J. Am. Chem. Soc.*, 2015, **137**, 8206–8218.
56 H. Qi, S. Mao, J. Rabeah, R. Qu, N. Yang, Z. Chen, F. Bourriquen, J. Yang, J. Li, K. Junge and M. Beller, *Angew. Chem., Int. Ed.*, 2023, **62**, e202311913.
57 A. Zhou, J. Huang, C. Zhao, Y. Fan, J. Qin, Q. Chen, M. He and W. Zhou, *Green Chem.*, 2024, **26**, 353–361.
58 C. Ma, C. Yang, H. Zhuo, C. Chen, K. Lu, F. Wang, Z. Shi, H. Xiao, M. Song and G. Jiang, *J. Am. Chem. Soc.*, 2023, **145**, 10890–10898.
59 Y. C. Deng, Z. C. Chen, J. N. Huang, G. X. Yang, Q. Zhang, Z. L. Liu, Y. H. Cao and F. Peng, *Chem. Eng. J.*, 2022, **444**, 136666.
60 Z. C. Chen, Y. H. Li, Y. H. Cao, Q. Zhang, H. Yu and F. Peng, *Int. J. Quantum Chem.*, 2021, **121**, e26780.
61 A. Nowacka, P. Briantais, C. Prestipinob and F. X. L. Xamena, *ACS Sustainable Chem. Eng.*, 2019, **7**, 7708–7715.
62 M. R. Maurya, U. Kumar and P. Manikandan, *Eur. J. Inorg. Chem.*, 2007, **16**, 2303–2314.